

Photoluminescent UV Light Modulation via Anisometric Carbon Nanodots for UV–Visible Shutter and UV Sensor

Mangesh D. Patekari, Archana Ramadas, Minhee Yun, Seung Hee Lee,* and MinSu Kim*

Carbon nanodots (CNDs) are promising photoluminescent nanomaterials due to their excellent optical properties, environmental benignity, and cost-effective synthesis from abundant precursors. However, their practical integration into optoelectronic devices is hindered by low synthetic yield, limited processability, and poor compatibility with host media. In contrast, liquid crystals offer electrical tunability and optical anisotropy, yet their potential in multifunctional platforms enabling simultaneous UV- and visible-light modulation remains underutilized. Here, the synthesis of anisometric CNDs and their incorporation into polymer network liquid crystals (PNLCs) are reported to construct a multifunctional optoelectronic system that exhibits UV–vis photoluminescence, light modulation, and UV sensing. The CNDs are uniformly aligned within nematic hosts, exhibiting broad UV absorption and polarized visible photoluminescence, with an emission dichroic ratio of ≈ 1.63 . The resulting hybrid film functions as UV–vis light shutters and photonic sensors, exhibiting $\approx 93.1\%$ transmittance and $\approx 8.4\%$ haziness in the transparent state, and switching to $\approx 13.3\%$ transmittance and $\approx 89.9\%$ haziness in the scattering state, with rapid response times (≈ 7.6 ms turn-on, ≈ 5.4 ms turn-off). Notably, the photoluminescence intensity is electrically and optically tunable, exhibiting a twofold change upon applied voltage and external UV exposure. This dual-responsive and polarized emission behaviors open new avenues for smart windows and adaptive optical technologies.

Among these, carbon nanodots (CNDs) have emerged as a compelling class of fluorescent nanomaterials due to their strong and tunable photoluminescence (PL), low cytotoxicity, environmental friendliness, and ease of synthesis from inexpensive carbon-rich precursors.^[1–8] Discovered serendipitously during the purification of single-walled carbon nanotubes,^[9] CNDs are typically quasi-spherical nanoparticles smaller than 10 nm, exhibiting size- and surface-dependent quantum confinement and emissive properties.^[2,10] Strategies such as heteroatom doping and surface passivation have been widely employed to enhance their fluorescence intensity and synthetic yield.^[4,11–14]

Concurrently, liquid crystal–based technologies have evolved from early studies of mesophase behavior into mature platforms widely deployed in advanced electro-optical devices. Composite systems such as polymer-dispersed liquid crystals (PDLCs)^[15–20] and polymer-network liquid crystals (PNLCs)^[21–27] enable electrically tunable light transmission by modulating refractive index contrast between aligned

and disordered liquid crystal domains. Among them, PNLCs offer superior optical transparency in the ground state by stabilizing homeotropic (perpendicular) alignment through polymer scaffolding. However, this typically requires the use of negative dielectric anisotropy liquid crystals to enable electrically driven reorientation into a scattering state.

1. Introduction

The development of advanced light-modulating materials has long been a cornerstone of materials science, driving innovations across optical, display, and sensing technologies. Recent progress in nanomaterials and liquid crystal science has enabled multifunctional systems with tunable optical properties.

M. D. Patekari, A. Ramadas, S. H. Lee, M. Kim
Department of Nano Convergence Engineering
Jeonbuk National University
Jeonju, Jeonbuk 54896, South Korea
E-mail: lsh1@jbnu.ac.kr; minsu.kim@jbnu.ac.kr

M. Yun
Department of Electrical and Computer Engineering
University of Pittsburgh
Pittsburgh, PA 15261, USA
S. H. Lee
Department of Polymer Nano Science and Technology
Jeonbuk National University
Jeonju, Jeonbuk 54896, South Korea
S. H. Lee
Department of JBNU-KIST Industry-Academia Convergence Research
Jeonbuk National University
Jeonju, Jeonbuk 54896, South Korea

The ORCID identification number(s) for the author(s) of this article can be found under <https://doi.org/10.1002/adfm.202514787>

© 2025 The Author(s). Advanced Functional Materials published by Wiley-VCH GmbH. This is an open access article under the terms of the [Creative Commons Attribution-NonCommercial-NoDerivs License](#), which permits use and distribution in any medium, provided the original work is properly cited, the use is non-commercial and no modifications or adaptations are made.

DOI: 10.1002/adfm.202514787

Although previous studies have demonstrated effective visible-light modulation in these liquid crystal composites, extending such control to the UV regime remains a significant technical challenge. Both PDLCs and PNLCs can deliver high optical contrast and rapid, reversible switching between transparent and opaque states, yet their performance in the UV spectrum is limited. Furthermore, PL properties have not been explored or integrated into these systems.

Attempts to modulate UV transmission using cholesteric liquid crystals have focused on tuning the helical pitch to reflect specific UV wavelengths. However, achieving the short pitch lengths required for UV reflection often demands high concentrations of chiral dopants, which can destabilize the liquid crystal phase, induce nonuniform helical structures, and narrow the reflection bandwidth. Additionally, cholesteric liquid crystals reflect only one circular polarization (left- or right-handed), resulting in at most 50% reflection of incident unpolarized light. Their angular sensitivity further limits broadband or omnidirectional applications. Moreover, cholesteric reflection is fundamentally low-absorption-based, which restricts its effectiveness for broadband UV filtering.^[28] To overcome these limitations, various nanoparticle-doped liquid crystal systems have been investigated. For example, Wang et al. introduced chemically functionalized titanium dioxide nanoparticles into PDLCs to enhance UV-shielding,^[29,30] while Zhao et al. reported zeolitic imidazolate framework-8-doped polymer-stabilized cholesteric liquid crystals for broadband UV attenuation.^[28] However, these approaches face persistent challenges in precise sub-band tuning, active switching, and long-term phase stability. The integration of UV-absorbing nanoparticles into liquid crystal matrices often leads to issues such as aggregation, phase separation, and reduced electro-optic performance.^[28–30]

Integrating CNDs into liquid crystal systems offers a compelling strategy to combine the broadband optical functionality of nanomaterials with the anisotropic alignment and voltage-tunable properties of liquid crystals. Our research addresses this critical gap by embedding CNDs into PNLCs, thereby enhancing UV modulation and extending the functional spectral range of liquid crystal-based devices. However, several technical barriers must be addressed to realize the practical application of this integration. First, conventional CND synthesis routes typically yield quantities insufficient for scalable device fabrication, particularly for applications such as smart windows. Second, the miscibility of CNDs with liquid crystal hosts is not inherently favorable, posing challenges to achieving stable, uniform alignment. To overcome these limitations, we developed a microwave-assisted synthesis method that employs a single-component nematic liquid crystal-based molecular precursor. This enables the direct in situ fabrication of CNDs within the host nematic phase. The resulting process is not only scalable and efficient but also exploits the intrinsic templating effect of the liquid crystal environment to guide the morphology and alignment of anisometric CNDs—a strategy previously demonstrated to be effective in directing nanostructure formation. This approach lays the groundwork for the next generation of UV-responsive, tunable optical devices.^[31–35]

The dual-phase evolution of light-modulating technologies—from the discovery of liquid crystal mesophases^[35–37] to the recent development of luminescent CNDs^[4,13,38–41]—has led to a new

generation of optoelectronic materials. CNDs, often referred to as “nanostructured brilliance”, exhibit their optical performance due to a combination of quantum confinement, surface state emissions, and anisotropic geometries.^[2,3,5,9,10,34,42] Among various fabrication methods for CNDs, microwave-assisted synthesis offers distinct advantages in terms of simplicity, rapid processing, and tunability of particle size and emission properties.^[34] In this study, we employed a single-molecule nematic liquid crystal precursor—4-cyano-4'-pentylbiphenyl (5CB)—to achieve controlled anisometric CND formation via microwave-assisted carbonization. The molecular structure of 5CB, which includes a rigid aromatic core, a polar cyano headgroup, and a flexible alkyl tail, promotes directional carbonization reactions under the influence of nematic ordering, yielding CNDs with structural anisotropy and narrow size distributions. This anisotropic morphology is critical for enabling directional optical responses such as polarized emission and tunable absorption. Moreover, the in situ synthesis within the LC host matrix ensures high miscibility and stable dispersion of the CNDs, effectively addressing common challenges of nanoparticle aggregation in functional composites. This approach not only simplifies processing by eliminating purification steps but also facilitates templated alignment of the CNDs through the orientational order of the liquid crystal. Previous studies have demonstrated that liquid crystal media can guide the alignment of nanoscale materials,^[43–45] and our work builds on this principle to enable multifunctional optoelectronic films with electrically and optically tunable properties.

Despite these promising developments, optimizing CND dispersion in the liquid crystal matrix and understanding the interfacial interactions within the PNLC network remain open challenges. Proper tuning of CND content, particle orientation, and liquid crystal–polymer interactions are essential to fully leverage their anisotropic optical properties. When properly aligned, both the anisometric CNDs and the birefringent liquid crystals contribute to field-responsive light modulation across an extended spectral range from UV to visible.

Our work demonstrates that integrating CNDs into PNLCs introduces a transformative feature: voltage-controllable, broadband modulation enabled by selective UV absorption and visible emission. This capability addresses the limitations of traditional PNLCs, which often transmit UV light unaltered regardless of their switching state. Governed by the Beer–Lambert law ($A = abc$, where A , a , b , and c are absorbance, molar absorptivity, length of light path, and concentration), the extent of light absorption is influenced by the concentration and path length of CNDs, providing an additional design parameter for optimizing performance.

The implications of this enhanced UV responsiveness are broad, particularly for UV-sensitive sensors. CND-doped PNLCs not only block harmful UV radiation but also emit quantifiable blue light upon excitation, making them suitable for environmental sensing, safety monitoring, and biomedical diagnostics. In this study, we describe the synthesis of anisometric CNDs using a microwave-assisted process and their integration into PNLC composites. We systematically evaluate the resulting electro-optical behavior and propose pathways for implementing these hybrid materials in adaptive optical devices such as smart windows, shutters, and next-generation optoelectronics. By addressing the fundamental challenges in CND–liquid crystal

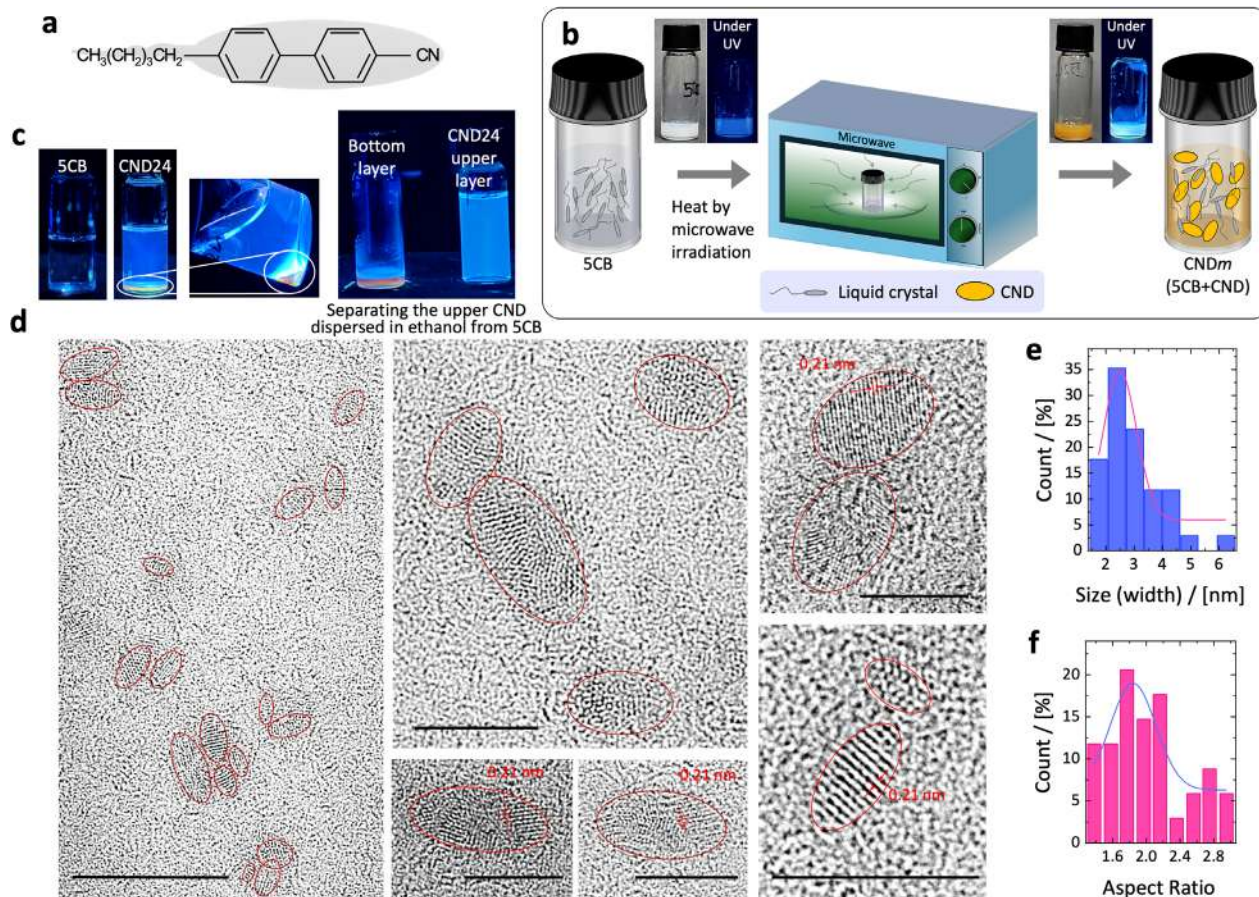


Figure 1. Microwave-assisted carbonization of 4-cyano-4'-pentylbiphenyl (5CB) to synthesize carbon nanodots (CNDs). a) Chemical structure of 5CB. b) Schematic illustration of the microwave-induced pyrolysis process leading to CND formation. Insets: Photographs of pristine 5CB and CND24 under ambient light (left) and 365 nm UV illumination (right), showing strong photoluminescence after carbonization. c) Extraction of the synthesized CNDs from CND24. d) High-resolution transmission electron microscopy (HRTEM) image of CND24 showing anisometric morphology. Scale bar: 5 nm. e) Size and f) aspect ratio distribution of CNDs, estimated from HRTEM images.

hybrid design, this work lays the foundation for new advances in light-modulating materials.

2. Results and Discussion

In this study, we successfully synthesized anisometric CNDs from a single-molecule liquid crystal precursor and employed these CND–liquid crystal mixtures to PNLC devices capable of converting UV light into visible PL. The CNDs exhibited linearly polarized emission, and their orientation within the nematic host matrix could be readily manipulated via an applied electric field. The synthesized CNDs dispersed uniformly in the host liquid crystal (5CB) without phase separation or aggregation, ensuring compatibility with PNLC fabrication and enabling direct application of the CND–liquid crystal mixture in device assembly.

2.1. Synthesis and Characterizations of CNDs in 5CB

We selected 4-cyano-4'-pentylbiphenyl (5CB; $C_{18}H_{19}N$, Figure 1a), a well-characterized thermotropic liquid crystal

exhibiting a nematic phase at room temperature, as the molecular precursor for the synthesis of carbon nanodots (CNDs). The synthesis procedure, schematically illustrated in Figure 1b, involved microwave-assisted pyrolysis conducted in a sealed, low-oxygen environment. This semi-inert atmosphere facilitated thermal fragmentation and partial oxidation of the precursor molecules while minimizing complete combustion. Although the detailed reaction mechanisms involved in microwave-assisted carbonization are complex and not fully elucidated, we hypothesize the following pathway based on detailed analysis of resultant CNDs, known principles of microwave-material interactions and thermal decomposition chemistry. Microwave irradiation is known to generate rapid, localized heating through dipolar polarization, particularly in molecules containing polar functional groups. In the case of 5CB, the polar cyano (–CN) group and the extended π -conjugated biphenyl framework act as effective microwave absorbers, enabling efficient volumetric heating. This localized energy input leads to the thermolysis of chemically labile sites, such as the aliphatic pentyl side chains and benzylic C–H bonds. The resulting carbon-centered radicals can undergo condensation, dehydrogenation, and aromatization reactions, thereby forming sp^2 -rich carbon domains.

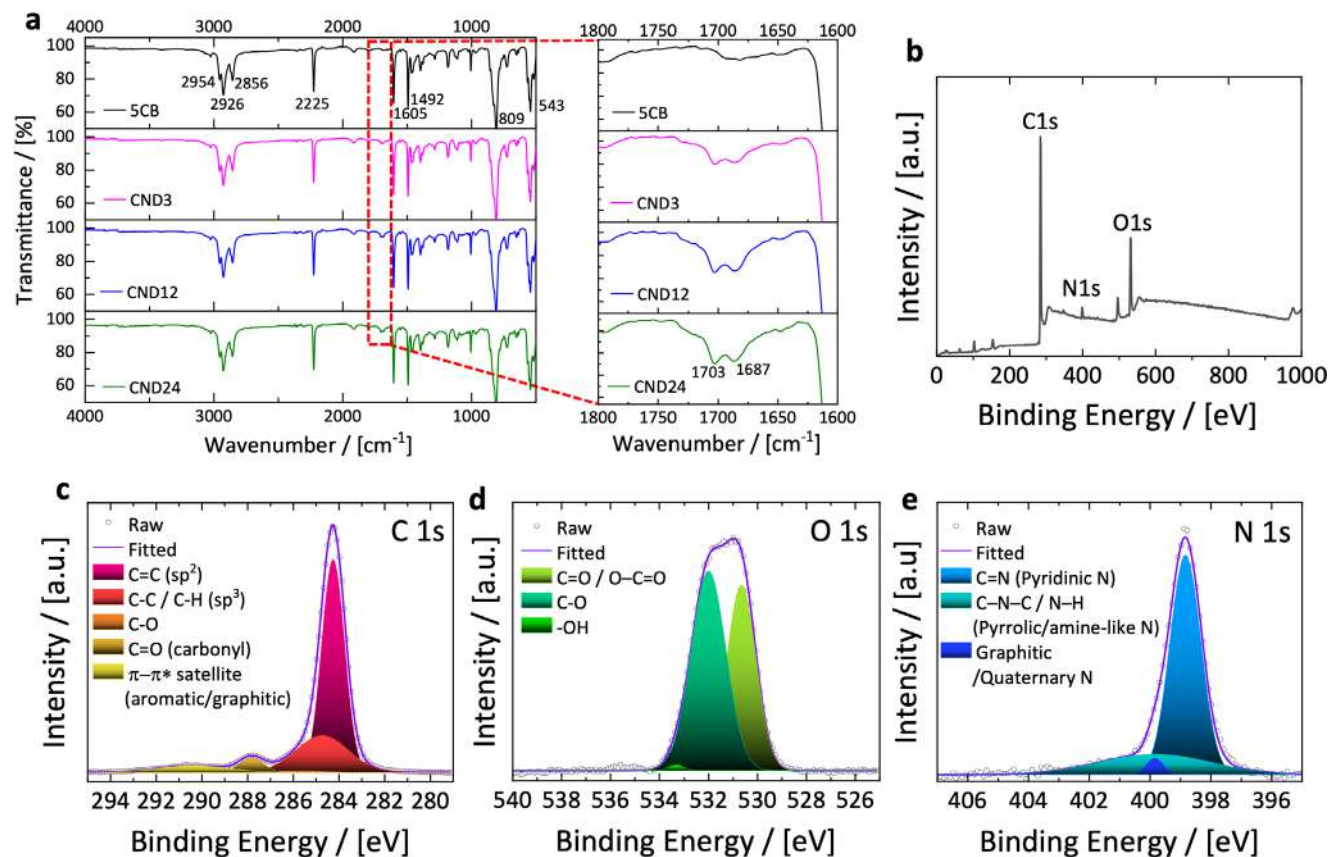


Figure 2. Chemical composition analysis of the extracted CNDs. a) Fourier-transform infrared (FTIR) spectra of 5CB, CND3, CND12, and CND24. Insets highlight the emergence of new vibrational bands at 1703 and 1687 cm⁻¹, attributed to C=O/C=N and C=C stretching modes, indicating progressive oxidation and aromatization. b–e) X-ray photoelectron spectroscopy (XPS) analysis of the extracted CNDs from CND24. (b) Survey spectrum showing the presence of carbon, oxygen, and nitrogen. (c) High-resolution C 1s spectrum showing peaks assigned to sp² C=C, sp³/aromatic C-C/C-H, C-O, C=O, and π-π* satellite shake-up transition in aromatic/graphitic systems. (d) O 1s spectrum indicating oxygen species including C=O/O=C=O, C-O, and -OH groups. (e) N 1s spectrum revealing nitrogen species including pyridinic N (C=N), pyrrolic/amine-like N (C-N-C/N-H), and graphitic/quaternary N.

Concurrently, the presence of trace oxygen within the sealed reaction vessel introduces surface functionalities such as hydroxyl, carbonyl, and nitrogen-containing groups, consistent with partial oxidative conditions. These transformations align with generally accepted carbonization mechanisms and are supported by our subsequent analyses.

The combination of microwave-induced molecular fragmentation, radical-driven recombination, and mild oxidation produces nanostructured carbonaceous materials with graphitic or amorphous domains characteristic of CNDs. The as-synthesized material exhibited a brownish-orange hue under ambient lighting and bright blue photoluminescence under 365 nm UV illumination, indicating successful formation of fluorescent carbon nanodots. For subsequent purification and characterization, we dispersed the as-prepared CND sample (designated as CND24) in ethanol, as shown in Figure 1c. Ethanol was chosen due to its ability to disrupt the original 5CB matrix and promote phase separation. Its strong hydrogen bonding network preferentially solvates the surface-functionalized, polar nanodots while excluding the hydrophobic 5CB molecules, which may undergo partial swelling. This procedure effectively separated CNDs from residual 5CB and allowed their collection in the polar solvent phase.

High-resolution transmission electron microscopy (HRTEM) revealed that the CNDs were anisometric in shape and exhibited clear lattice fringes with a spacing of ≈0.21 nm, corresponding to the (100) in-plane lattice spacing of graphitic carbon (Figure 1d). Statistical analysis of numerous individual nanodots yielded an average particle diameter of 3 ± 1.12 nm and an average aspect ratio of 2 ± 0.47, as shown in Figure 1e,f.

The chemical composition of 5CB, CND3, CND12, and CND24 was analyzed using FTIR spectroscopy (Figure 2a), which reveals molecular transformations during the carbonization of 5CB, although interpretation may be partially limited by the coexistence of unconverted 5CB. Pristine 5CB exhibits characteristic peaks including C-H stretching vibrations (2850–2950 cm⁻¹), C≡N stretching at 2225 cm⁻¹, aromatic C=C stretching (1492 and 1605 cm⁻¹), and out-of-plane C-H bending of the benzene ring at 809 cm⁻¹, consistent with its known molecular structure. After microwave irradiation, new absorption bands appeared at 1703 and 1687 cm⁻¹, corresponding to C=O/C=N and C=C stretching modes, respectively. These new peaks suggest the formation of oxygen- and nitrogen-containing functional groups, which are commonly observed in partially oxidized carbon nanostructures such as graphene oxide, indicating successful functionalization

during the synthesis. The source of oxygen is likely trace amounts of residual atmospheric oxygen in the sealed reaction vial.

More detailed insights into the surface chemical states of the extracted CNs were obtained via X-ray photoelectron spectroscopy (XPS) (Figure 2b–e). The survey scan (Figure 2b) revealed the presence of carbon (C 1s at 284.26 eV, 82.19%), oxygen (O 1s at 531.26 eV, 14.67%), and nitrogen (N 1s at 398.85 eV, 3.13%). This composition confirms a predominantly carbonaceous structure with notable incorporation of oxygen and nitrogen, originating from the carbonization of 5CB. The high-resolution C 1s spectrum (Figure 2c) was deconvoluted into multiple components: a strong peak at 284.1 eV assigned to sp²-hybridized graphitic carbon (C=C), a peak at 284.7 eV corresponding to aliphatic/aromatic C–C or C–H, and a signal at 286.1 eV attributed to C–O and/or C–N bonding, indicative of oxidized or nitrogen-doped carbon species. A peak at 287.8 eV reflects carbonyl (C=O) functionalities, and a distinct π – π^* shake-up satellite at 290.5 eV indicates extended aromatic conjugation, typical of partially graphitized carbon networks. The O 1s spectrum (Figure 2d) includes three principal contributions: a peak at 531.0 eV attributed to carbonyl and carboxyl oxygen (C=O / O–C=O), a dominant peak at 532.4 eV corresponding to C–O (e.g., hydroxyl or ether groups), and a minor shoulder at 532.9 eV assigned to hydroxyl groups (–OH). These oxygenated species likely arose from oxidation processes during microwave treatment in a semi-sealed environment. The N 1s spectrum (Figure 2e) shows three distinct peaks: a prominent peak at 398.8 eV from pyridinic nitrogen (C=N), a broader peak at 399.9 eV corresponding to pyrrolic or amine-like nitrogen (C–N–C / N–H), and a smaller signal at 401.6 eV ascribed to graphitic or quaternary nitrogen. These nitrogen functionalities likely originate from the nitrile (–CN) group of 5CB and were incorporated during carbonization, contributing to surface passivation and possibly enhancing the photoluminescent properties of the CNs.^[34,46,47]

2.2. Optical Properties of 5CB and CNs

To investigate the optical behavior of the synthesized CNs, we compared pristine 5CB and synthesized CN samples under UV light (Figure 3a) and in two solvents: acetone and chloroform (Figure 3b,c). CN24 exhibited a markedly enhanced blue emission under 365 nm UV illumination, in contrast to the negligible fluorescence of pristine 5CB. Uniform dispersions of 5CB, CN3, CN12, and CN24 were prepared in both solvents at a concentration of 0.25 wt.% via 5 min of sonication. As the number of microwave treatment cycles increased, the PL intensity improved accordingly, indicating progressive carbonization and CN formation (Figure S1a,b, Supporting Information).

PL spectra excited at 360 nm (Figure S1c,d, Supporting Information) confirmed that pristine 5CB exhibited minimal emission, while CN24 demonstrated significantly enhanced blue fluorescence. This enhancement was further corroborated by UV–visible absorption and PL emission spectroscopy (Figure 3d–i) for three different sample conditions: neat (no solvent, Figure 3a,d,g), dispersed in acetone (Figure 3b,e,h), and dispersed in chloroform (Figure 3c,f,i). The CN24 samples showed stronger and broader absorption and emission features

compared to 5CB, with blue emission being particularly prominent. Notably, CNs dispersed in chloroform (Figure 3i) exhibited stronger PL intensity than those in acetone (Figure 3h). This enhancement can be attributed to solvent effects on the CN electronic structure, including interactions that influence radiative recombination pathways. The measured PLQYs of CN24 were 28% in acetone and 44% in chloroform (Figure S2, Supporting Information), suggesting that solvent polarity and molecular interactions play a critical role in emission efficiency—stronger solute–solvent interactions can lead to enhanced nonradiative decay pathways, thereby reducing PLQY.^[48] Additional PL spectra (Figures S3 and S4, Supporting Information) further illustrate how emission properties evolve with microwave irradiation, confirming CN formation. The PL behavior was excitation-wavelength-dependent, a characteristic feature of carbon-based nanomaterials. As excitation wavelength increased, emission peaks shifted to longer wavelengths (redshift), indicative of heterogeneous emissive sites. For CN24, this shift was subtle, suggesting relatively narrow size and emissive site distributions (Figure 3g). In contrast, pristine 5CB showed weak, excitation-dependent emission (Figure 3d), which diminished as CNs formed with increasing irradiation cycles (Figure S5, Supporting Information).

Solvent-dependent variations in emission were also explored. CNs in acetone exhibited a mixed emission profile, with dominant blue and secondary green emission components. This dual emission likely arises from solvent effects on the surface electronic states of the CNs, including interactions with polar functional groups, defect states, and oxygenated moieties.^[49,50] The observed variation in PLQY between chloroform and acetone for the CN24 dispersion is attributed not solely to general solvent polarity, but also to distinct molecular-level interactions involving hydrogen bonding,^[51,52] dipolar effects,^[52,53] and excited-state stabilization.^[54,55] While the CNs in CN24 are partially shielded by 5CB and exhibit relatively low surface polarity due to limited oxygen incorporation during synthesis, residual functional groups—such as carbonyl or amine moieties—remain available for interaction with surrounding solvent molecules. Acetone, a polar aprotic solvent with a high hydrogen bond accepting capability (Kamlet–Taft $\beta \approx 0.48$) and high dipolarity/polarizability ($\pi^* \approx 0.71$),^[56,57] can interact with these polar surface groups via dipole–dipole or hydrogen bonding interactions. Such interactions are known to stabilize excited states and reduce the energy gap between the excited and ground states, thereby facilitating non-radiative decay and resulting in lower PLQY. In contrast, chloroform, a weakly polar solvent with minimal hydrogen bonding ability ($\beta \approx 0.10$, $\pi^* \approx 0.58$),^[56,57] exhibits limited interaction with the CN surface, suppressing non-radiative relaxation and favoring radiative recombination. These findings are consistent with previously reported solvent-dependent photophysical behaviors of CNs and highlight that both solvent polarity and specific solvation interactions influence the optical performance.^[54,55] Although direct quantification of solvation free energy or hydrogen bonding index for this system is unavailable, the observed solvatochromic red shift and the PLQY difference align with solvent-induced excited-state modulation, as supported by established polarity scales and literature precedents.

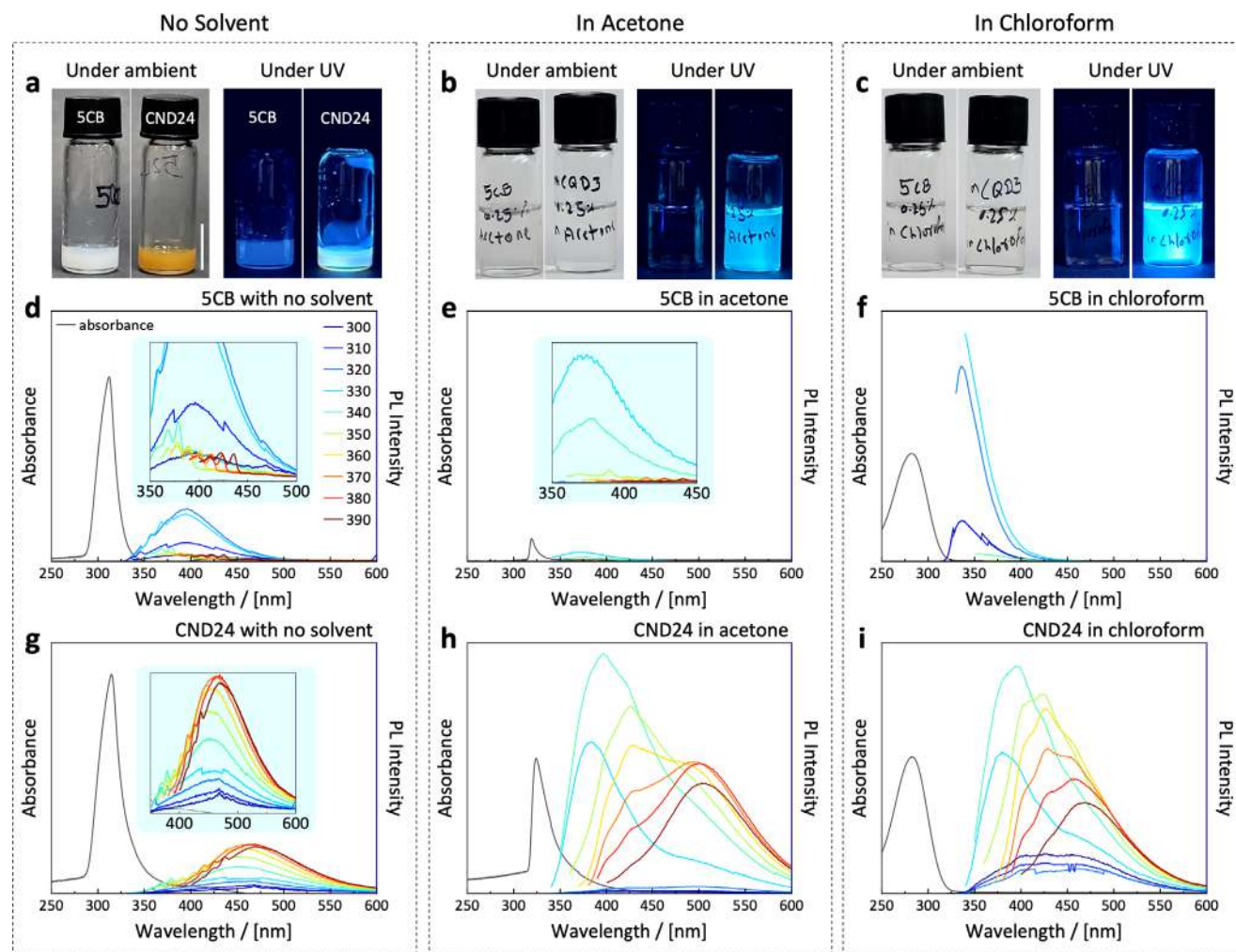


Figure 3. Photographic and spectroscopic comparison of pristine 5CB and CND24. a–c) Photographic images of samples under ambient and UV light (365 nm), dispersed in (a) neat form, (b) acetone, and (c) chloroform. Scale bar: 1 cm. d–f) UV–vis absorption and PL emission spectra of (d) neat, (e) acetone-dispersed, and (f) chloroform-dispersed 5CB. g–i) UV–vis absorption and PL emission spectra of corresponding samples in (g) neat, (h) acetone, and (i) chloroform-dispersed CND24, measured at excitation wavelengths ranging from 300 to 390 nm.

2.3. Polarized Emission Properties and Electric Field Switching of CNDs

The linearly polarized PL of CNDs was examined using PFM and PFS. (Details on the cell fabrication and alignment procedure are provided in the Experimental Section.) Figure 4a,b shows PFM images of homogeneously aligned cells containing CND24. When the polarizer is aligned parallel to the rubbing direction (Figure 4a), strong blue emission is observed, while a significant reduction in intensity is seen when the polarizer is rotated perpendicular to the rubbing direction (Figure 4b), indicating anisotropic, polarization-dependent PL.

This behavior is attributed to the alignment of anisometric CNDs along the nematic director of the 5CB host, which is templated by the rubbing-induced surface grooves. The alignment mechanism is consistent with prior studies on anisotropic nanoparticles, such as gold nanorods and quantum rods, which also align along the liquid crystal director due to elastic energy minimization and Van der Waals or π - π interaction between

nanorods and liquid crystal molecules.^[58–60] The rubbing process, widely used in liquid crystal displays, effectively orients both liquid crystal molecules and embedded anisotropic nanomaterials across macroscopic areas.

PFS measurements further support this alignment behavior. As shown in the schematic (Figure 4c), a single polarizer was rotated within the sample plane to probe angular-dependent PL intensity. The spectral response (Figure 4d) exhibits a maximum when the polarizer is parallel to the rubbing direction and a minimum when perpendicular, consistent with the macroscopically aligned anisometric CNDs. In contrast, samples without rubbing treatment (Figure 4e) or with randomly aligned CNDs in PNLC matrices (Figure 4f) show markedly reduced angular dependence, confirming that the polarized PL originates from directional alignment within the nematic host. These results confirm that the anisometric shape of the CNDs, combined with the orientational templating provided by the nematic liquid crystal, enables directional alignment and polarization-sensitive PL emission, which is not observed in randomly oriented systems.

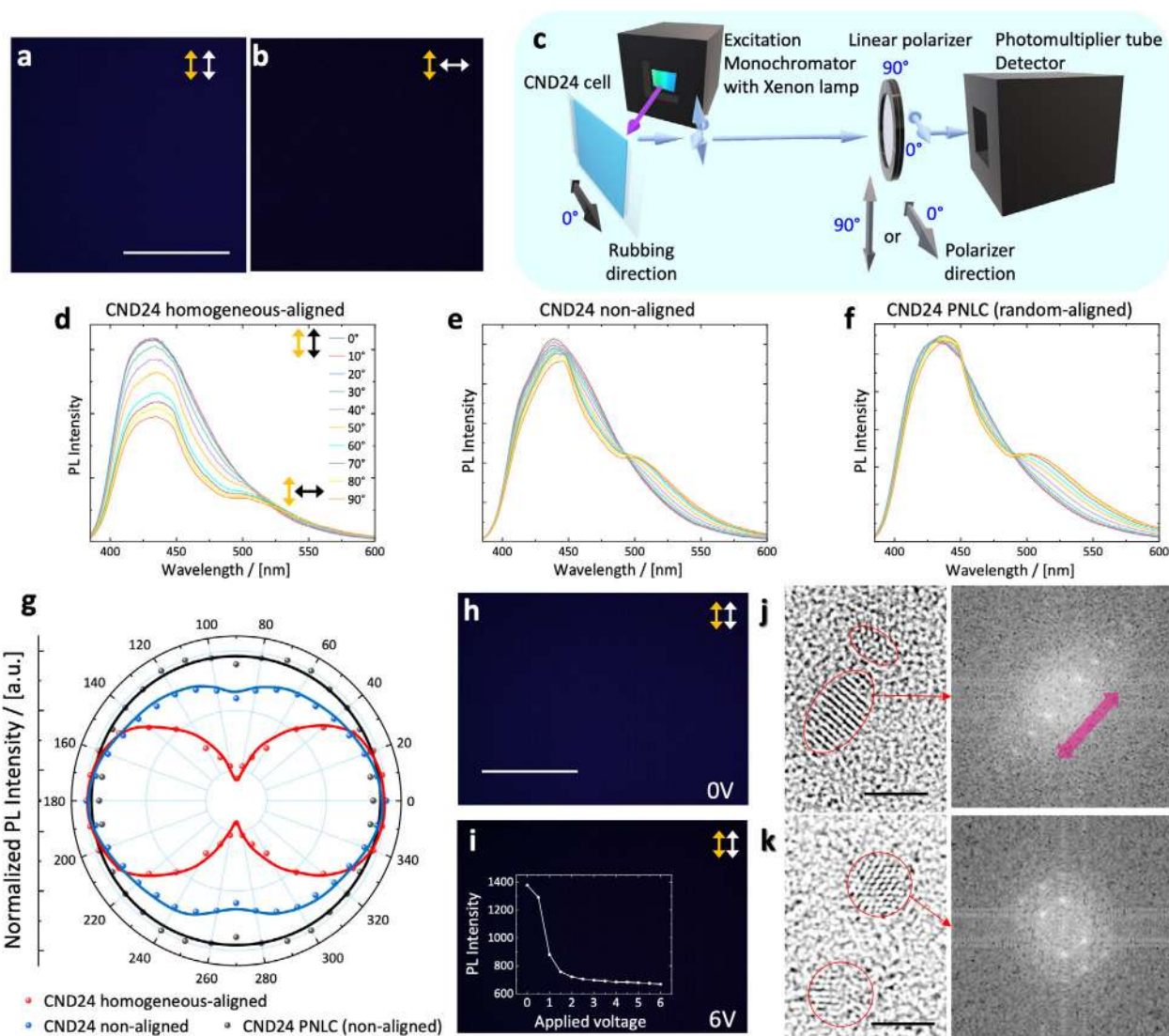


Figure 4. Azimuthal angle-resolved PL emission for polarized emission and electric field modulation of homogeneously aligned CND24. a,b) Polarized fluorescence microscopy (PFM) images of CND24 in planar-aligned cells under UV excitation. White arrows indicate polarizer orientation; yellow arrows indicate the rubbing direction. The scale bar is 400 μm . c) Schematic of polarized fluorescence spectroscopy (PFS) setup. d–f) Polarized PL spectra of CND24 in (d) homogeneously (planarly-uniform) aligned, (e) non-aligned, and (f) randomly aligned polymer-networked liquid crystal (PNLC) samples, measured at 370 nm excitation and 450 nm emission. g) Polar plots of PL intensity, measured at 370 nm excitation and 450 nm emission, as a function of polarization angle for the three sample types. (Red contour line) Homogeneously (planarly-uniform) aligned. (Blue contour line) Non-aligned. (Black contour line) Randomly aligned PNLC samples. h,i) PFM images of homogeneously aligned CND24 at (h) 0 V and (i) 6 V, showing reduced emission due to electric field-induced molecular reorientation. Inset: voltage-dependent PL intensity (maximum values extracted from Figure S8, Supporting Information). Yellow arrows indicate rubbing direction; white/black arrows indicate polarizer orientation. The scale bar is 400 μm . j,k) Fast-fourier transition images (right column) from HRTEM images (left column) of (j) the extracted anisometric CNDs from CND24 and (k) quasi-spherical CNDs synthesized, using resorcinol as a precursor by a solvothermal method (See Figure S10, Supporting Information). The scale bars are 2 nm. The magenta pink arrow in (j) indicates the anisotropic domain orientation, which is absent in (k).

Typically, isometric CNDs emit unpolarized PL that does not vary with analyzer rotation. However, for these anisometric CNDs, the PL is strongly polarized due to the alignment of transition dipole moments along their longer axis, resulting in clear angular dependence. On the other hand, when an aligning electric field is applied vertically (perpendicular to the plane) or anisometric CNDs are randomly dispersed within polymer matrix, the CNDs reorient such that their shape appears quasi-isometric from the top view, minimizing in-plane anisotropy; un-

der this condition, the PL spectrum remains identical when rotating the analyzer from 0° to 90°.

Quantitative analysis of PL intensity at 450 nm (excited at 370 nm) was used to construct polar plots for the three configurations (Figure 4g). Homogeneously aligned CND24 exhibits a pronounced elliptical distribution, whereas non-aligned samples show more isotropic profiles. A slight angular dependence observed in the non-aligned case (blue curve) is attributed to subtle flow alignment effects induced during capillary injection. The

Table 1. Polarization PL properties of CND24 with different conditions.

Nos.	P_{\parallel}	P_{\perp}	$P_{\parallel} / P_{\perp}$	$R = (P_{\parallel} - P_{\perp}) / (P_{\parallel} + 2P_{\perp})$	$p = (P_{\parallel} - P_{\perp}) / (P_{\parallel} + P_{\perp})$	Alignment conditions
1	319.95	195.97	1.63	0.17	0.24	CND24 homogeneous-aligned
2	514.37	458.12	1.12	0.03	0.05	CND24 non-aligned
3	534.29	533.52	1.00	0.00047	0.00071	CND24 PNLC random-aligned

observed polarization-dependent emission confirms that the anisometric CND24 structures possess intrinsic dichroic optical properties. Using PL intensity values parallel (P_{\parallel}) and perpendicular (P_{\perp}) to the rubbing direction, we calculated the emission dichroic ratio ($D = P_{\parallel} / P_{\perp}$), the optical anisotropy parameter ($R = (P_{\parallel} - P_{\perp}) / (P_{\parallel} + 2P_{\perp})$), and the polarization ratio ($p = (P_{\parallel} - P_{\perp}) / (P_{\parallel} + P_{\perp})$). For the homogeneously aligned CND24, these values were $D \approx 1.63$, $R \approx 0.17$, and $p \approx 0.24$, as summarized in **Table 1**.

To investigate electric field responsiveness, we leveraged the positive dielectric anisotropy of 5CB (≈ 10 at 20 °C, 1 kHz), which favors alignment of its long molecular axis parallel to the applied electric field. PFM images taken at 0 and 6 V (Figure 4h,i) clearly show that the PL emission in CND24 decreases with voltage application. At 0 V, the sample emits blue light under parallel polarizers, confirming planar (homogeneous) alignment. Upon application of 6 V, the emission is significantly reduced, suggesting that the CND24 molecules have reoriented into a vertical (homeotropic) alignment due to the electric field. This transition disrupts the alignment between the emission dipoles and the polarizer, thereby diminishing the detected PL intensity. The inset of Figure 4i shows the measured decrease in PL intensity from ≈ 1377 at 432 to ≈ 692 at 419 nm (maximum values extracted from Figure S8, Supporting Information with the PL setup as shown in Figure S9, Supporting Information) as a function of increasing voltage, further supporting the electrically tunable anisotropic behavior of CND24 in the nematic host.

To elucidate the origin of polarized PL in the synthesized CNDs, we examined the relationship between particle geometry, internal structural order, and local electronic dipole alignment. HRTEM coupled with fast Fourier transform FFT analysis was performed on both anisometric CNDs derived from 5CB (Figure 4j) and isotropic CNDs synthesized from resorcinol via a solvothermal route we followed the method found in the reference^[61] (Figure 4k; Figure S10, Supporting Information). Despite their overall amorphous carbon matrix, both samples exhibit distinct quasi-crystalline features. In particular, both CNDs show evidence of partial long-range ordering within the particle body, consistent with the distribution of localized sp^2 -conjugated regions embedded in a predominantly sp^3 -carbon network. These π -conjugated nanodomains act as quantum-confined emissive centers, each possessing a transition dipole moment aligned with the local π -axis. In isotropic particles, the spatial orientation of these domains is unoriented, leading to cancellation of dipole directions at the ensemble level and resulting in unpolarized PL. However, in the anisometric CNDs, the elongated geometry favors partial alignment of sp^2 -domains along the long axis, likely facilitated by the directional carbonization kinetics and molecular packing templated by the 5CB liquid

crystal environment. This shape-induced domain alignment promotes collective orientation of transition dipoles, giving rise to observable polarized PL. Thus, the polarization behavior arises not from long-range crystallinity, but from the cooperative interplay between particle anisotropy, internal π -domain alignment, and host-assisted orientation, despite the quasi-amorphous character of the overall lattice structure.

2.4. Polymer Network Formation and Optical Modulation in PNLC Cells

As illustrated schematically in **Figure 5a**, PNLC cells were fabricated using 5CB or CND24 as the host nematic liquid crystal, with the reactive mesogen RM257 (Figure 5b) and the photoinitiator Irgacure 651 (Figure 5c). The polymer network was formed via PIPS between ITO-coated glass substrates (details in the Experimental Section). In conventional PDLCs, high polymer concentrations (> 30 wt.%) are typically required to induce sufficient scattering, but this compromises optical absorbance due to reduced liquid crystal content per unit thickness, as described by the Beer–Lambert law. To maintain high absorbance while enabling effective scattering, we set the polymer concentration below 6 wt.%. At such low concentrations, however, 5CB-based cells fail to produce a uniform scattering state due to incomplete polymer network formation, as typically seen in PDLCs.

Interestingly, when polymerization of the RM257 mixed with CND24, a markedly different optical behavior was observed. Although the CND24-based mixture initially exhibited vertical alignment under homeotropic conditions, the PIPS process resulted in a well-dispersed and strongly scattering state after curing. This transition is attributed to multiple interrelated factors. First, the CNDs may disrupt the vertical alignment of the liquid crystal molecules during polymerization through surface-mediated interactions. Functional groups present on the CND surfaces—such as hydroxyl, carbonyl, carboxyl, and nitrogen-containing moieties—can interact with surrounding 5CB and RM257 molecules via van der Waals forces or π - π stacking. These interactions are particularly influential near the alignment surfaces, where they may interfere with the anchoring conditions and destabilize the initial director configuration. Second, the relatively low UV light intensity used during photopolymerization (irrelative to the absorbance wavelength of a photoinitiator) (Figure S11, Supporting Information) may result in a slower polymer network formation. This slower kinetics allows greater possibility of polymer chain formation during the curing process, increasing the likelihood of anchoring disruptions and misalignment. Collectively, these effects promote the formation of a disordered molecular arrangement stabilized by the polymer matrix.

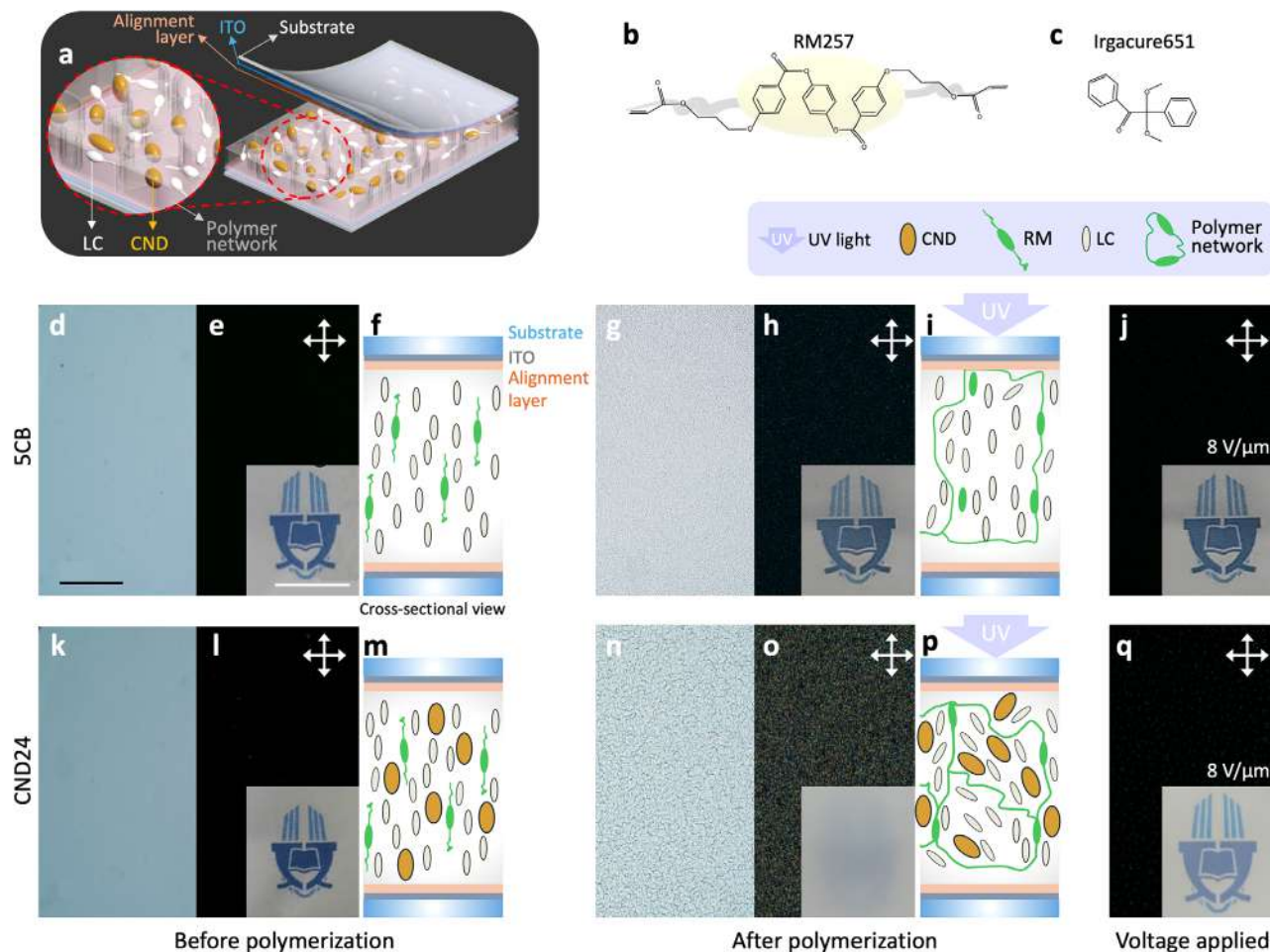


Figure 5. Fabrication and characterization of PNLC cells via photo-polymerization. a) Schematic of PNLC cell structure. b,c) Chemical structures of (b) reactive mesogen RM257 and (c) photoinitiator Irgacure 651. d–j) Images of 5CB-based PNLC cells before (d–f) and after (g–i) photopolymerization: (d,g) optical microscopy (OM) images, (e,h,i) POM images, and (f,j) schematic cross sections. k–q) Corresponding images for CND24-based PNLC cells: (k,n) OM, (l,o,q) POM, (m,p) schematic cross sections. j,q) POM images after applying voltage ($8 \text{ V } \mu\text{m}^{-1}$). Insets in (e,h,j,l,o,q) show corresponding photographic images under ambient light. White arrows indicate crossed polarizer directions. Scale bars: $200 \mu\text{m}$ (microscopy), 1 cm (photographs).

The resulting refractive index mismatch between misaligned liquid crystal domains and the polymer network gives rise to a macroscopically scattering texture in the ground state. The polymer-networked liquid crystal alignment formation is compared in Figure 5d–q, where PNLC cells with 5CB (Figure 5d–j) and CND24 (Figure 5k–q) are analyzed using an optical microscopy (OM) and POM, both before and after PIPS. Prior to curing, both systems appear transparent under OM (Figure 5d,k) and dark under crossed polarizers (Figure 5e,l), indicating uniform alignment. However, after curing, 5CB-based cells remain optically clear and aligned (Figure 5h), with no apparent polymer scattering (Figure 5i), as schematically shown in Figure 5f,m. In contrast, CND24-based PNLCs develop a pronounced scattering state (Figure 5o) despite beginning in a vertically aligned configuration, as schematically shown in Figure 5p.

Additional trials using various alignment layers confirmed the consistency of this effect: CND24 reproducibly produced a well-dispersed scattering state after PIPS, while 5CB did not (Figures S12–S15, Supporting Information). Before PIPS, both types of cells appeared transparent to the naked eye, as

shown in the photographic insets of Figure 5e,l. After PIPS, only the CND24-based PNLC exhibits significant optical scattering, leading to an opaque appearance (photographic inset of Figure 5o). Upon applying an electric field of $8 \text{ V } \mu\text{m}^{-1}$, both systems switch to a homeotropic alignment, resulting in a dark field under POM (Figure 5j,q) and visually transparent appearance (photographic inset of Figure 5q). The result unequivocally demonstrates the electric field-responsive switching behavior of both PNLC configurations—yet critically, only the CND24-based PNLC achieves a high-scattering off-state, enabling significantly enhanced optical contrast and superior performance in light modulation applications.

2.5. Spectral and Optical Properties of the CND24-Based UV-Visible Shutter and UV Sensor

The CND24-based PNLC device functions as both a UV–vis light shutter and a UV sensor, enabling dynamic optical modulation and light-sensitive emission. To investigate its performance, we

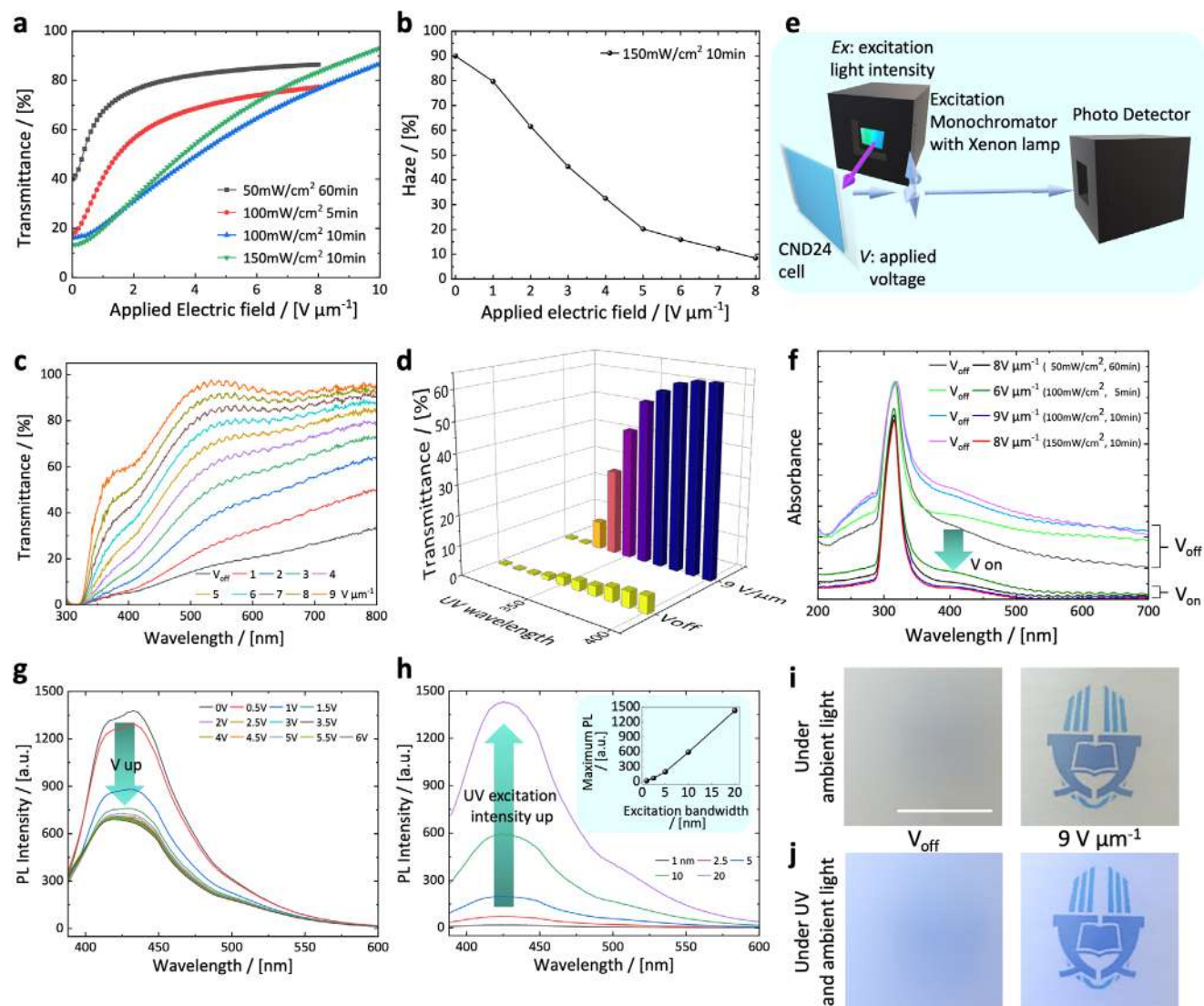


Figure 6. Electro-optic and optoelectronic characterization of the CND24-based PNLC shutter and UV sensor. a) Electric field strength-dependent transmittance in various UV irradiation condition. b) Haziness of a PNLC sample under optimized UV condition. c) UV-vis spectra at different electric field strengths. d) Transmittance changes for demonstration of shutter effect between voltage-off (V_{off}) and voltage-on ($V = 9 \text{ V } \mu\text{m}^{-1}$). e) Schematic of the optical measurement setup. f) Absorbance spectra of PNLC cells when switching between V_{off} and V_{on} . g) Voltage-dependent PL spectra. h) Excitation intensity-dependent PL behavior (excitation intensity vary by changing bandwidths); inset shows peak PL intensity versus excitation intensity (bandwidth). i, j) Photographs of PNLC device over a printed background: (i) ambient light only; (j) ambient + UV light, showing bluish PL. V_{off} (First column); $V = 9 \text{ V } \mu\text{m}^{-1}$ (second column). Scale bar: 1 cm.

evaluated electro-optic behavior as a function of UV curing conditions, particularly varying UV irradiance and exposure time (see Figure 6a and Table 2; corresponding images in Figure S16, Supporting Information). The UV curing setup is shown in Figure S17 (Supporting Information).

As UV irradiance increases, the resulting polymer domains become smaller and more finely dispersed. This leads to decreased transmittance in the voltage-off state and increased transmittance under applied voltage ($V = 8 \text{ V } \mu\text{m}^{-1}$), due to more efficient field-induced reorientation of the liquid crystals. The best contrast ratio ($\text{CR} = 7.02$) was achieved with a UV irradiance of 150 mW cm^{-2} for 10 min, although this sample required a higher operating voltage due to the tighter polymer network

(Figure 6a). The haziness (transmittance), which reflects scattering efficiency, range from $\approx 89.9\%$ ($\approx 13.3\%$) at voltage-off state to $\approx 8.4\%$ ($\approx 93.1\%$) at $V = 8 \text{ V } \mu\text{m}^{-1}$, as shown in Figure 6b.

The thickness of the CND24-based PNLC layer directly influences its light scattering, PL intensity, and operating voltage. According to the Beer-Lambert law, a greater optical path length (i.e., thicker cell) increases both scattering and PL emission due to enhanced light-matter interaction. However, since the electric field strength is defined as $E = V/d$ where d is the cell thickness, a thicker cell requires a proportionally higher driving voltage to achieve the same field strength for molecular reorientation.

The device clearly exhibits reversible transmittance modulation across both UV and visible wavelengths (Figure 6c). The

Table 2. Optical shutter properties of PNLC CND24 cells under different UV curing conditions.

UV irradiance/ [mW cm ⁻²]	UV irradiation time/ [min]	Transmittance (Haziness) at V _{off} /[%]	Transmittance (Haziness) at 8 V μm ⁻¹ /[%]	Contrast ratio (CR)
50	60	39.96	86.49	2.16
100	5	17.90	77.31	4.31
150	10	13.25 (89.9)	93.06 (8.4)	7.02

broadband optical switching behavior of the device was confirmed via UV–vis transmittance measurements under varying applied fields (Figure 6d), using the photonic setup in Figure 6e. The photoresponsive properties of CND24 were further evaluated through absorbance and PL emission analyses. Figure 6f shows field-dependent absorbance spectra: applying voltage causes the CND24 alignment to switch from random to homeotropic, decreasing light absorption due to reduced optical path length and orientation-dependent effects. Full UV–vis spectral data under applied voltage and different UV conditions for PIPS are provided in Figures S18 and S19 (Supporting Information).

Importantly, the CND24 PNLC exhibits UV shutter and UV sensor functionality. The full PL emission spectra of 5CB and CND24-based PNLC cells are compared in Figure S20 (Supporting Information). As applying voltage changes, PL emission intensity is decreased significantly as shown in Figure 6g, measured with the setup illustrated in Figure S9 (Supporting Information). In addition, as excitation intensity increases (modulated by varying slit width in the optical setup in Figure 6e), the PL intensity increases proportionally (Figure 6h), validating the device’s sensitivity to UV intensity. The inset in Figure 6h shows the excitation intensity-dependent PL maxima. Photographic images of the device on a patterned background under ambient light (Figure 6i) and combined ambient + UV light (365 nm, Figure 6j)

illustrate this multi-functionality. In the voltage-off state (left column), the shutter appears opaque, obscuring the background. Under UV illumination, the device exhibits a visible bluish glow due to PL emission from CND24. The bluish color is a result of UV-triggered emission and is not directly related to scattering-induced haziness. Additional photographic comparisons under different UV curing conditions are provided in Figure S21 (Supporting Information).

2.6. Mechanism of Optical Switching in PNLC Cells

The switching behavior of the fabricated PNLC cells using 5CB and CND24 is schematically illustrated in Figure 7. Cross-sectional views from Figure 5i (5CB) and Figure 5p (CND24) are reinterpreted here to highlight the director responses under UV–vis light and applied electric fields. In the 5CB-based PNLC cell, the vertically aligned liquid crystal director allows UV–vis light to pass through with minimal interaction, resulting in a clear, transparent state in the absence of voltage (Figure 7a). When a vertical electric field is applied, the molecular orientation remains largely unchanged—aligned parallel to the field—thus maintaining the transparent state (Figure 7b). In contrast, the CND24-based PNLC cell exhibits a distinct switching mechanism due to the incorporation of anisometric CNDs. During

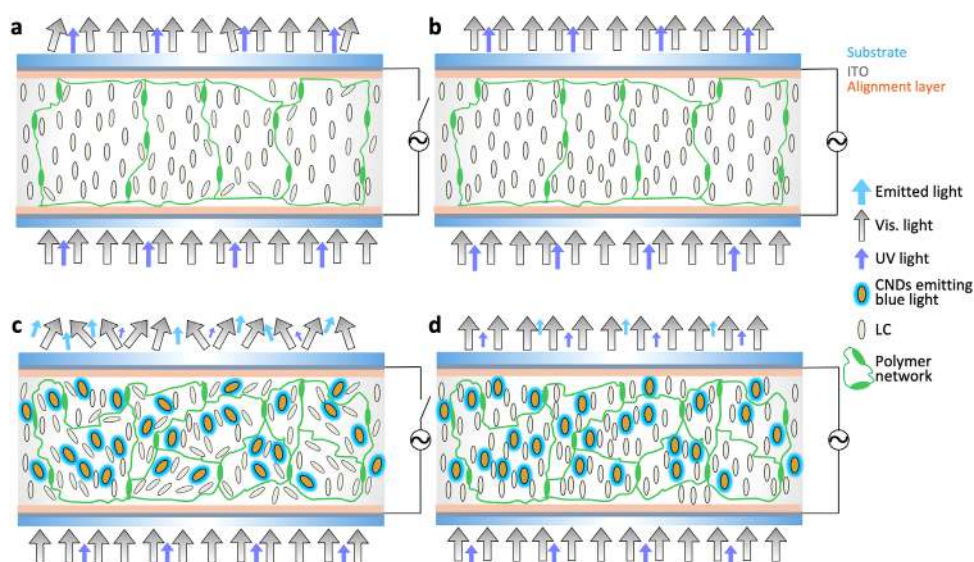


Figure 7. Schematic illustration of the optical switching mechanism in polymerized PNLC cells. a,b) 5CB-based PNLC cells under (a) V_{off} and (b) V_{on} conditions c,d) CND24-based PNLC cells under (c) V_{off} and (d) V_{on} conditions. The direction of molecular alignment and light interaction pathways are indicated.

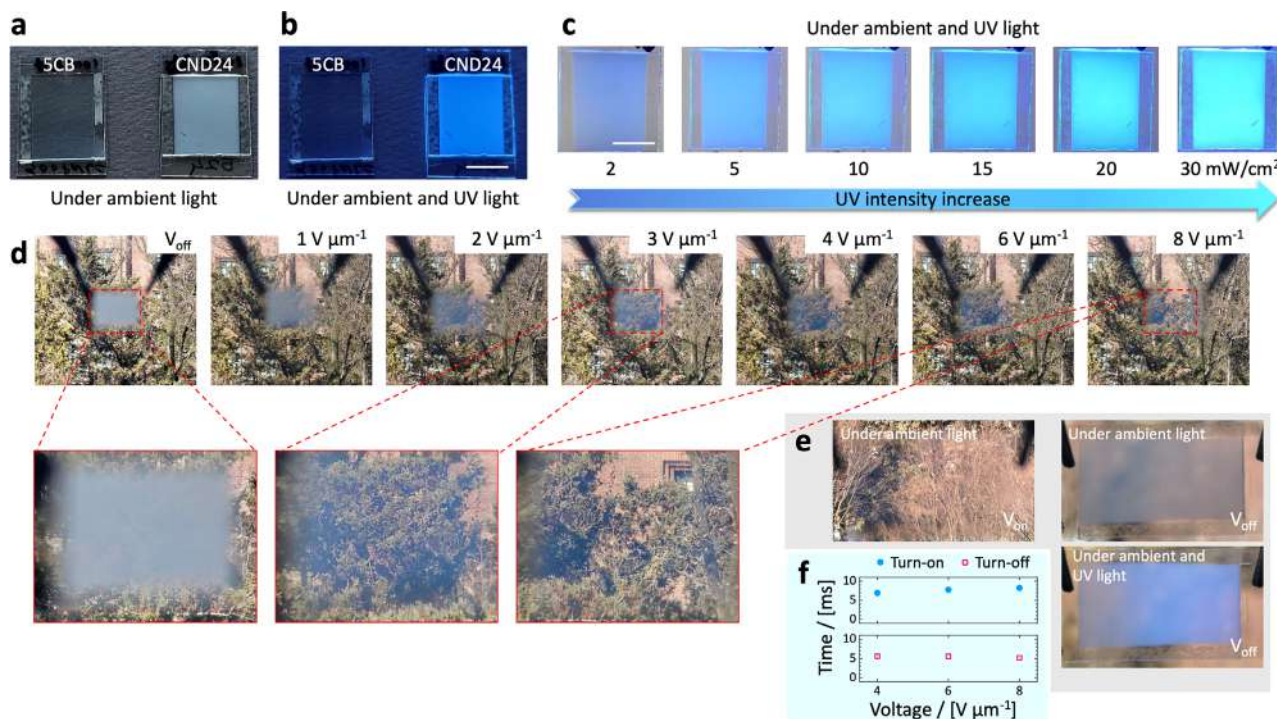


Figure 8. Performance demonstration of CND24-based PNLC UV shutter and sensor. a,b) Photographs of 5CB and CND24 PNLC cells under (a) ambient light and (b) UV light. c) Emission response of the CND24 PNLC cell under increasing UV intensity. Scale bars: 1 cm. d) Voltage-induced transparency modulation of the CND24 PNLC under ambient light (0–8 V μm^{-1}). Close-up images in red-dotted rectangles show transition from opaque to transparent with increasing voltage (0, 3, 8 V μm^{-1}). e) Switching properties of the CND24 PNLC under ambient and UV light: (Left-up) transparent under V_{on} , (Right-up) opaque under V_{off} , and (Right-down) opaque with visible bluish PL under combined ambient and UV light at V_{off} . f) Response times of the CND24 PNLC cell at various voltage application.

photopolymerization, both 5CB molecules and the anisometric CNDs disrupt the initial vertical alignment and the initial alignment at voltage-off state becomes randomly oriented. The liquid crystal director and polymer network structural mismatch causes significant optical scattering, primarily due to the refractive index mismatch between misaligned liquid crystal domains and the polymer matrix. At the same time, the randomly oriented CNDs absorb incident UV light and re-emit it as PL. Therefore, the voltage-off state appears hazy and emissive, driven by a combination of light scattering (from refractive index mismatch) and UV absorption/PL (from CNDs) (Figure 7c). Upon application of an external electric field, the liquid crystal director realigns along the field direction. Due to π - π interaction and van der Waals interactions, the anisometric CNDs also tend to align along the reoriented liquid crystal director. This co-alignment leads to improved optical uniformity and refractive index matching (as both the RM257 and 5CB possess ordinary refractive indices, n_o near 1.5), thereby reducing scattering. In addition, the reorientation of the CNDs results in their π -conjugated axes—and thus their transition dipole moments—becoming aligned perpendicular to the observation direction, which suppresses the effective PL intensity. Consequently, the voltage-on state exhibits high optical transparency and reduced emission, arising from diminished scattering and directional suppression of CND photoluminescence (Figure 7d).

The functional performance of the fabricated PNLC devices is demonstrated in Figure 8. Under ambient light, 5CB cell ap-

pears transparent while CND24 cell appears opaque (Figure 8a), but under additional UV illumination, the CND24 cell distinctly emits bluish light due to its photoluminescent response (Figure 8b). This bluish light confirms effective UV absorption and emission by CNDs embedded in the polymer network. As the intensity of incident UV light increases, the bluish emission from the CND24 PNLC becomes more pronounced (Figure 8c), illustrating its UV-sensitive photonic behavior. This behavior validates the potential application of the system as a visual UV sensor.

To further demonstrate the multi-functionality of the device as a smart UV-vis shutter, the CND24 PNLC cell was mounted on a transparent window and subjected to varying electric fields under ambient light (Figure 8d). In the absence of voltage, the cell exhibits an opaque state due to light scattering. As the applied voltage increases (up to 8 V μm^{-1}), the cell transitions into a transparent state. This voltage-dependent opacity modulation is clearly shown in the photographic insets. In Figure 8e, the switching properties of the CND24 PNLC under ambient and UV light is demonstrated: under ambient light with voltage applied (Left-up), the cell appears transparent; when the voltage is removed (Right-up), it returns to an opaque state. Under UV light in the voltage-off state (Right-down), the cell not only becomes opaque but also emits a visible bluish glow, reinforcing its multi-functionality as both a shutter and a UV-responsive sensor.

The response times of the CND24 PNLC cell were evaluated as illustrated in Figure 8f. At applied field strengths of 4, 6, and

$8 \text{ V } \mu\text{m}^{-1}$, the average turn-on and turn-off times were measured to be $\approx 7.6 \pm 0.6$ and 5.4 ± 0.2 ms, respectively. From an application standpoint, these response times are comparable to those of conventional nematic liquid crystals, demonstrating the potential of CND24 PNLC cells for fast-switching electro-optic and optoelectronic devices and sensors.

3. Conclusion

This study presents a transformative strategy for the development of multifunctional light-responsive materials by synthesizing anisometric carbon nanodots (CNDs) directly from a single-component nematic liquid crystal precursor (5CB) using a scalable, microwave-assisted carbonization method. The resulting CNDs exhibit intrinsic shape anisotropy, strong blue photoluminescence, and broad UV absorption, while remaining highly dispersible within the liquid crystal host—overcoming longstanding limitations in nanodot processability and compatibility.

By integrating these CNDs into polymer network liquid crystals (PNLCs), we demonstrate the first hybrid optoelectronic platform that simultaneously achieves electrically tunable light modulation and UV-responsive photoluminescence. The system exhibits rapid voltage-induced switching between transparent ($\approx 93.1\%$ transmittance) and scattering ($\approx 13.3\%$ transmittance) states with sub-10 ms response times, alongside polarized visible emission (dichroic ratio ≈ 1.63) that is dynamically modulated by both electric fields and UV light. Notably, the CNDs enhance polymer network formation during photopolymerization, enabling effective light scattering at ultralow polymer content—an effect not observed in CND-free control samples.

Beyond the optoelectronic performance, this work reveals the mechanistic role of particle shape, internal π -domain orientation, and nematic templating in driving polarized PL from quasi-amorphous nanodots—establishing a novel design paradigm for anisotropic nanocarbon materials. The dual stimuli-responsiveness, scalable synthesis, and intrinsic alignment compatibility mark a significant advancement in light-manipulating soft matter systems.

This CND–PNLC hybrid architecture thus offers a versatile platform for next-generation smart windows, wearable UV sensors, adaptive displays, and dynamic optical shutters. More broadly, the approach sets the stage for future integration of soft-assembled nanocarbons in tunable photonic and optoelectronic systems, uniting nanomaterials chemistry, liquid crystal physics, and device engineering in a single framework.

4. Experimental Section

Synthesis of Carbon Nanodots (CNDs): CNDs were synthesized using 4-cyano-4'-pentylbiphenyl (5CB, see Figure 1a) as a single-component liquid crystalline precursor. The precursor was carbonized via microwave irradiation, resulting in the formation of CNDs from 5CB. The synthesis was performed by placing neat 5CB into a sealed glass vial, followed by irradiation in a commercial microwave oven (800 W power, Figure 1b). Each microwave cycle consisted of 1 min of irradiation followed by a 1-min rest period to prevent sample degradation due to overheating. Increasing the m number of cycles led to a higher degree of carbonization and increased CND content within the 5CB host. The optimized sample (optimizing procedure shown in Figure S22, Supporting Information), denoted as CND24, was synthesized using $m = 24$ cycles (totaling 48 min, including rest in-

tervals). Untreated 5CB is referred to as 5CB, while samples treated with 3 and 12 cycles are denoted as CND3 and CND12, respectively, as m in CND m denotes the number of cycles.

Extraction of CNDs from 5CB: The CND24 mixture was treated with ethanol to induce phase separation, which was visibly apparent even before vortexing as shown in Figure 1c and Figure S23 (Supporting Information), as initial aggregation of 5CB was observed. The sample was then vortexed for 2 min to promote uniform mixing of the CNDs in ethanol. Following this, the mixture was placed in the deep freezer compartment of a standard refrigerator, maintained at ≈ -18 °C, for a total of 2 h to facilitate further aggregation and settling of the 5CB at the bottom, while the CNDs remained dispersed in the ethanolic supernatant. After removal from the freezer, the upper layer containing CNDs in ethanol was carefully collected and passed through a $0.1 \mu\text{m}$ vacuum filtration unit, followed by centrifugation at 12,000 rpm for 10 min. These steps were carried out to remove any remaining large particles and ensure a more refined CND dispersion. These steps were carried out multiple times, trying to remove a maximum of 5CB. The filtered and centrifuged CND suspension was then used for subsequent characterization or processing. Utilizing a deep freezer at -18 °C enhances the efficiency of 5CB aggregation and phase separation before collection, while filtration and centrifugation further purify the CND fraction. Even after filtration, a small amount of 5CB may remain with the CNDs in ethanol due to its molecular size and partial dispersibility in ethanol; however, its overall quantity is significantly reduced.

Photoluminescence Quantum Yield (PLQY): PLQY measurements were conducted using a spectrofluorometer (FluoroMax Plus, Horiba) equipped with an integrating sphere (QuantaPhi 2 PLQY, Horiba; 121 mm internal diameter, 250–1700 nm reflectivity). Samples were dissolved in acetone or chloroform and adjusted to yield an absorbance of 0.05–0.1 at the excitation wavelength. Blank measurements were also performed using pure solvents. Samples were excited with UV light between 320 and 330 nm, and emissions were collected over the 300–550 nm range. Excitation and emission slits were set to 3 nm, with an integration time of 0.1 s. Measurements were performed using a standard quartz fluorescence cuvette. PLQY was calculated using the Horiba FluorEssence software, based on the equation $PLQY = \frac{E_c - (1-A)E_b}{L_a A} = \frac{E_c - E_a}{L_a - L_c}$, where E_c and E_a are the fluorescence emissions of the sample and blank; L_c and L_a represent excitation scattering from the sample and blank, respectively; E_b is the integrated luminescence from the sample caused by indirect luminescence caused by the sphere; and A is the sample absorbance at the excitation wavelength.^[62] The Fourier transform infrared (FTIR) analysis was conducted using a FTIR spectrometer (FT/IR-4100, Jasco).

Preparation of Homogeneously Aligned Liquid Crystal Cells: To fabricate planar-aligned CND m liquid crystal cells, indium tin oxide (ITO)-coated glass substrates were sequentially cleaned and spin-coated with polyimide at 600 rpm for 20 s and 2000 rpm for 70 s. The coated substrates were pre-baked at 80 °C for 20 s and post-baked at 230 °C for 16 min. A rubbing process was then applied by dragging a velvet cloth across a polymer-coated substrate, creating micro-grooves that guide the alignment of LC molecules in azimuthal direction through surface interactions. Two substrates were assembled with anti-parallel rubbing directions, separated by $10 \mu\text{m}$ Mylar spacers. The alignment layers induced the alignment of the host liquid crystal as well as the synthesized anisometric CND m mixtures, which were introduced into the cells via capillary action.

Fabrication of Polymer Network Liquid Crystal (PNLC) Cells: PNLC composites were prepared using CND24, reactive mesogen RM257 (Merck; $n_e = 1.687$, $n_o = 1.508$), and the photoinitiator Irgacure 651 (Sigma-Aldrich). The Irgacure 651 was 0.5 wt.% relative to RM257. The final mixture composition was CND24: RM257 + Irgacure 651 = 94: 6 (wt.%). A reference sample using untreated 5CB was also prepared (5CB: RM257 + Irgacure 651 = 94: 6). These mixtures were filled into cells identical in design to those above, except with vertical (homeotropic) alignment layers for PNLC configurations. Homeotropic alignment was achieved to vertically orient the liquid crystal and RM257 molecules. After cell assembly, polymerization-induced phase separation (PIPS) was initiated by irradiating the samples with 365 nm UV light.

Characterization Techniques: High-resolution transmission electron microscopy (HRTEM) analysis was performed on a high-resolution

instrument (Titan Cubed G2 60–300 and Talos F200X G2, FEI) to observe the nanostructure and morphology of the synthesized CNDs. The surface chemical composition was examined by X-ray photoelectron spectroscopy using an X-ray photoelectron spectrometer (Nexsa, ThermoFisher Scientific). Polarizing optical microscopy (POM) was employed to observe liquid crystal alignment and electro-optic response. Polarizing fluorescence microscopy (PFM) images were acquired in reflection mode using a POM (Eclipse TE 2000-U, Nikon) equipped with a CCD camera (LWD 0.52, Nikon). UV–vis absorption spectra were obtained using a UV–vis spectrophotometer (ARSN-733, Jasco), while transmittance in the 300–1000 nm range was measured using another UV–vis system (S-3100, Scinco). PL spectra were recorded with a spectrofluorophotometer (RF-6000, Shimadzu) and time-correlated single-photon counting (TCSPC) setup (Fluorolog-3, Horiba) in the unit of counts per second (CPS). Polarized fluorescence spectroscopy (PFS) was performed by placing a linear polarizer in front of the detector. The excitation wavelengths used for PFM and PFS were 365 and 370 nm, respectively. Electro-optic response was analyzed using a liquid crystal measurement system (LCMS 200, Sesim Photonics Technology). UV light intensity at 365 nm was measured using a UV meter (UIT-250, Ushio). Visible-range haze as a function of applied voltage was measured using a haze meter (UV-3600i, Shimadzu).

Supporting Information

Supporting Information is available from the Wiley Online Library or from the author.

Acknowledgements

This work was supported by Basic Science Research Program through the National Research Foundation (NRF) of Korea, funded by the Ministry of Science and ICT (MSIT), Korea [2022R1A2C2091671]; by the Technology Innovation Program, funded by the Ministry of Trade, Industry & Energy (MOTIE), Korea [20022529]; and by BK21 FOUR Program by Jeonbuk National University Research Grant. The authors thank to Shin-Woong Kang and Jinseck Kim for valuable discussions.

Conflict of Interest

The authors declare no conflict of interest.

Author Contributions

M.D.P. conducted the experiments, analyzed data, and wrote the manuscript. M.Y. consulted the idea. S.H.L. initiated the project and edited the manuscript. M.S.K. conceived the idea, conducted the experiments, analyzed data, and wrote, and edited the manuscript. M.S.K. and S.H.L. performed conceptualization, supervision, wrote, reviewed, and edited the draft, and funding acquisition. M.D.P., A.R., and M.S.K. performed methodology and investigation. M.D.P. and M.S.K. performed visualization and wrote the original draft.

Data Availability Statement

The data that support the findings of this study are available from the corresponding author upon reasonable request.

Keywords

anisometric CNDs, carbon nanodots (CNDs), polarized emission, UV–visible light modulation, UV sensors

Received: June 11, 2025

Revised: August 3, 2025

Published online:

- [1] C. Liu, P. Zhang, F. Tian, W. Li, F. Li, W. Liu, *J. Mater. Chem.* **2011**, *21*, 13163.
- [2] Y. Park, J. Yoo, B. Lim, W. Kwon, S. W. Rhee, *J. Mater. Chem. A* **2016**, *4*, 11582.
- [3] L. Zhang, X. Yang, Z. Yin, L. Sun, *Luminescence* **2022**, *37*, 1612.
- [4] L. Li, T. Dong, *J. Mater. Chem. C* **2018**, *6*, 7944.
- [5] S. Y. Lim, W. Shen, Z. Gao, *Chem. Soc. Rev.* **2014**, *44*, 362.
- [6] M. R. Hasan, N. Saha, T. Quaid, M. Toufiq Reza, *Energies (Basel)* **2021**, *14*, 986.
- [7] Y. Wang, Y. Zhu, S. Yu, C. Jiang, *RSC Adv.* **2017**, *7*, 40973.
- [8] L. Wang, W. Li, L. Yin, Y. Liu, H. Guo, J. Lai, Y. Han, G. Li, M. Li, J. Zhang, R. Vajtai, P. M. Ajayan, M. Wu, *Sci. Adv.* **2020**, *6*, eabb6772.
- [9] X. Xu, R. Ray, Y. Gu, H. J. Ploehn, L. Gearheart, K. Raker, W. A. Scrivens, *J. Am. Chem. Soc.* **2004**, *126*, 12736.
- [10] A. Dutta, S. T. Y. Trolles-Cavalcante, A. Cleetus, V. Marks, A. Schechter, R. D. Webster, A. Borenstein, *Nanoscale Adv.* **2021**, *3*, 716.
- [11] R. J. P. Latiza, J. Olay, C. Eguico, R. J. Yan, R. V. Rubi, *J. Mater. Sci.* **2025**, *60*, 5006.
- [12] D. Sengottuvelu, A. K. Shaik, S. Mishra, H. Ahmad, M. Abbaszadeh, N. I. Hammer, S. Kundu, *ACS Omega* **2022**, *7*, 27742.
- [13] Ö. K. Koç, A. Üzer, R. Apak, *ACS Appl. Mater. Interfaces* **2023**, *15*, 42066.
- [14] M. Azami, J. Wei, M. Valizadehderakhshan, A. Jayapalan, O. O. Ayodele, K. Nowlin, *J. Phys. Chem. C* **2023**, *127*, 7360.
- [15] M. S. Kim, D. Y. Lee, H. Y. Jung, S. H. Lee, *Composites, Part B* **2024**, *278*, 111425.
- [16] S. Pagidi, M. S. Kim, R. Manda, S. Ahn, M. Y. Jeon, S. H. Lee, *J. Mol. Liq.* **2023**, *380*, 121730.
- [17] S. Pagidi, R. Manda, H. S. Shin, J. Lee, Y. J. Lim, M. S. Kim, S. H. Lee, *J. Mol. Liq.* **2021**, *322*, 114959.
- [18] S. Pagidi, H. S. Park, D. Y. Lee, M. S. Kim, S. H. Lee, *J. Mol. Liq.* **2022**, *350*, 118540.
- [19] N. H. Park, S. C. Noh, P. Nayek, M.-H. Lee, M. S. Kim, L.-C. Chien, J. H. Lee, B. K. Kim, S. H. Lee, *Liq. Cryst.* **2015**, *42*, 530.
- [20] M. Kim, B. G. Kang, M. S. Kim, M. K. Kim, P. Kumar, M. H. Lee, S. W. Kang, S. H. Lee, *Curr. Appl. Phys.* **2010**, *10*, 118.
- [21] Y. J. Lim, M. Kang, H. S. Jeon, M. S. Kim, S. H. Lee, *J. Mol. Liq.* **2022**, *368*, 120823.
- [22] M. S. Kim, Liquid Crystalline Amorphous Blue Phase: Tangled Topological Defects, Polymer-stabilization, and Device Application, **2015**.
- [23] Y. J. Lim, J. H. Lee, G. Y. Lee, M. Jo, E. J. Kim, T. H. Kim, M. S. Kim, M.-H. Lee, S. H. Lee, *J. Mol. Liq.* **2021**, *340*, 117302.
- [24] R. Manda, S. Pagidi, M. S. Kim, C. H. Park, H. S. Yoo, K. Sandeep, Y. J. Lim, S. H. Lee, *Liq. Cryst.* **2018**, *45*, 736.
- [25] M. S. Kim, R. K. Mishra, R. Manda, G. Murali, T.-H. Kim, M.-H. Lee, M. Yun, S. Kundu, B.-S. Kim, S. H. Lee, *RSC Adv.* **2017**, *7*, 16650.
- [26] S. S. Gandhi, M. S. Kim, J.-Y. Hwang, L.-C. Chien, *Adv. Mater.* **2016**, *28*, 8998.
- [27] R. Manda, M. S. Kim, E. J. Shin, M. S. Gong, G. Murali, K. Sandeep, M. H. Lee, J. H. Lee, S. H. Lee, *Liq. Cryst.* **2017**, *44*, 1059.
- [28] Y. Zhao, D. Yang, Y. Lu, K. Li, Z. Guo, J. Gao, R. Yao, D. Wang, Y. Luan, H. Gao, *Battery Energy* **2025**, 20240078.
- [29] X. Wang, W. Hu, H. Chen, M. H. Saeed, J. Huang, J. Hu, Y. Ren, J. Xu, L. Zhang, M. Yu, H. Zhang, H. Yang, *Polym. Adv. Technol.* **2022**, *33*, 1561.
- [30] S. Agarwal, S. Srivastava, S. Joshi, S. Tripathi, B. P. Singh, K. K. Pandey, R. Manohar, *ACS Mater. Au* **2025**, *5*, 88.
- [31] M. C. Rath, S. K. Sarkar, V. K. Wadhawan, R. Verma, I. M. L. Das, R. Dąbrowski, M. Tykarska, R. Dhar, *Opto-Electron. Rev.* **2008**, *16*, 399.
- [32] V. Gdovinová, M. A. Schroer, N. Tomašovičová, I. Appel, S. Behrens, J. Majorošová, J. Kováč, D. I. Svergun, P. Kopčanský, *Soft Matter* **2017**, *13*, 7890.
- [33] C. Da Cruz, O. Sandre, V. Cabuil, *J. Phys. Chem. B* **2005**, *109*, 14292.

- [34] S. Subedi, A. K. Rella, L. G. Trung, V. Kumar, S. W. Kang, *ACS Nano* **2022**, *16*, 6480.
- [35] G. R. Meseck, A. S. Terpstra, M. J. MacLachlan, *Curr. Opin. Colloid Interface Sci.* **2017**, *29*, 9.
- [36] M. Mitov, *ChemPhysChem* **2014**, *15*, 1245.
- [37] T. Hanemann, W. Haase, I. Svoboda, H. Fuess, *Liq. Cryst.* **1995**, *19*, 699.
- [38] D. Sengottuvelu, A. K. Shaik, S. Mishra, H. Ahmad, M. Abbaszadeh, N. I. Hammer, S. Kundu, *ACS Omega* **2022**, *7*, 27742.
- [39] M. S. Zaini, J. Y. C. Liew, S. Paiman, T. S. Tee, M. A. Kamarudin, *J. Fluoresc.* **2023**, *35*, 245.
- [40] P. M. Gharat, J. M. Chethodil, A. P. Srivastava, P. K. Praseetha, H. Pal, S. D Choudhury, *Photochem. Photobiol. Sci.* **2019**, *18*, 110.
- [41] O. Dimitriev, D. Kysil, A. Zaderko, O. Isaieva, A. Vasin, Y. Piryatinski, M. Fahlman, A. Nazarov, *Nanoscale Adv.* **2024**, *6*, 2185.
- [42] K. Dimos, *Curr. Org. Chem.* **2015**, *20*, 682.
- [43] T. Hanemann, W. Haase, I. Svoboda, H. Fuess, *Liq. Cryst.* **1995**, *19*, 699.
- [44] C. Da Cruz, O. Sandre, V. Cabuil, *J. Phys. Chem. B* **2005**, *109*, 14292.
- [45] V. Gdovinová, M. A. Schroer, N. Tomašovičová, I. Appel, S. Behrens, J. Majorošová, J. Kováč, D. I. Svergun, P. Kopčanský, *Soft Matter* **2017**, *13*, 7890.
- [46] A. A. Astafiev, A. M. Shakhov, A. G. Tskhovrebov, A. Shatov, A. Gulín, D. Shepel, V. A. Nadtochenko, *ACS Omega* **2022**, *7*, 6810.
- [47] X. Zhang, Y. Liu, C. H. Kuan, L. Tang, T. D. Krueger, S. Yeasmin, A. Ullah, C. Fang, L. J. Cheng, *J. Mater. Chem. C Mater.* **2023**, *11*, 11476.
- [48] S. A. Cherevkov, E. A. Stepanidenko, M. D. Miruschenko, A. M. Zverkov, A. M. Mitroshin, I. V. Margaryan, I. G. Spiridonov, D. V. Danilov, A. V. Koroleva, E. V. Zhizhin, M. V. Baidakova, R. V. Sokolov, M. A. Sandzhieva, E. V. Ushakova, A. L. Rogach, *J. Mater. Chem. C Mater.* **2024**, *12*, 3943.
- [49] O. Dimitriev, D. Kysil, A. Zaderko, O. Isaieva, A. Vasin, Y. Piryatinski, M. Fahlman, A. Nazarov, *Nanoscale Adv.* **2024**, *6*, 2185.
- [50] D. Sengottuvelu, A. K. Shaik, S. Mishra, H. Ahmad, M. Abbaszadeh, N. I. Hammer, S. Kundu, *ACS Omega* **2022**, *7*, 27742.
- [51] T. Steiner, *New J. Chem.* **1998**, *22*, 1099.
- [52] S. Mukherjee, E. Prasad, A. Chadha, *Phys. Chem. Chem. Phys.* **2017**, *19*, 7288.
- [53] A. T. Krasley, E. Li, J. M. Galeana, C. Bulumulla, A. G. Beyene, G. S. Demirer, *Chem. Rev.* **2024**, *124*, 3085.
- [54] P. W. Carr, *Microchem. J.* **1993**, *48*, 4.
- [55] F. Arshad, A. Pal, M. A. Rahman, M. Ali, J. A. Khan, M. P. Sk, *New J. Chem.* **2018**, *42*, 19837.
- [56] R. W. Taft, M. J. Kamlet, *J. Am. Chem. Soc.* **1976**, *98*, 2886.
- [57] M. J. Kamlet, R. W. Taft, *J. Am. Chem. Soc.* **1976**, *98*, 377.
- [58] Q. Liu, Y. Yuan, I. I. Smalyukh, *Nano Lett.* **2014**, *14*, 4071.
- [59] S. Kaur, G. Murali, R. Manda, Y. Cheol Chae, M. Yun, J. Hee Lee, S. Hee Lee, S. Kaur, R. Manda, Y. C. Chae, J. H. Lee, S. H. Lee, M. Yun, *Adv. Opt. Mater.* **2018**, *6*, 1800235.
- [60] C. J. Dintinger, B.-J. Tang, X. Zeng, F. Liu, T. Kienzler, G. H. Mehl, G. Ungar, C. Rockstuhl, T. Scharf, J. Dintinger, T. Scharf, B. Tang, G. H. Mehl, X. B. Zeng, F. Liu, G. Ungar, T. Kienzler, C. Rockstuhl, *Adv. Mater.* **2013**, *25*, 1999.
- [61] F. Yuan, P. He, Z. Xi, X. Li, Y. Li, H. Zhong, L. Fan, S. Yang, *Nano Res.* **2019**, *12*, 1669.
- [62] What are Luminescence Quantum Yields? - HORIBA.